Functional Characteristics of Ultrasonic Shot-peened Ti–Ni Shape Memory Alloy with Functionally Graded Property

Ryosuke Matsui[*]

Department of Mechanical Engineering, Aichi Institute of Technology,
1247 Yachigusa, Yakusa-cho, Toyota, Aichi 470-0392, Japan

The author aimed to enhance the functional characteristics of the proposed Ti–Ni shape memory alloy (SMA) with a functionally graded property by ultrasonic shot peening (USP) treatment. To the author's knowledge, this was the first study in which USP treatment was utilized for manufacturing functionally graded SMAs; previous studies relied on powder metallurgy and hot rolling techniques. By examining the various properties of the specimens, the author confirmed the effects of hot rolling and USP treatment. Hot rolling and USP treatment led to an increased Vickers hardness. Hot rolling primarily contributed to densification, while USP treatment induced work hardening, resulting in increased hardness. The surface of TiNi SMA sintered bodies experienced compressive residual stress up to 300 MPa because of the USP treatment. The transformation peaks in differential scanning calorimetry curves shifted toward lower temperatures as the Ni content increased. Therefore, the transformation properties of the functionally graded shape memory alloys were unaffected by the USP treatment. The USP treatment work-hardens the sintered TiNi SMA produced through hot rolling. The effect was more pronounced in the high-Ni-concentration region, resulting in the development of a functionally graded behavior of deformation resistance.

1. Introduction

Shape memory alloys (SMAs) exhibit two characteristics known as the shape memory effect and superelasticity, which are affected by temperature.[1,2] The shape memory effect enables the recovery of large deformations through heating, while superelasticity enables the recovery of large deformations without heating. Consequently, SMAs exhibit functional properties that are not present in other metal materials. These shape memory properties are observed in various series of alloy, with Ti–Ni based SMAs (TiNi SMAs) being particularly notable for their fatigue strength, corrosion resistance, and biocompatibility. Consequently, they are widely employed in various fields, ranging from medical devices, such as stents and guidewires, to a diverse range of coil-spring-shaped actuators equipped with temperature sensors.[3,4]

In TiNi SMAs, the shape memory characteristics fundamentally arise from the martensitic transformation of the parent austenite phase and its reverse transformation. For instance, when TiNi SMAs are deformed, stress-induced martensitic transformation occurs. During the subsequent heating process, shape recovery starts at the beginning of the reverse transformation and continues until the completion of the reverse transformation. Therefore, the transition temperatures and functional properties of TiNi SMAs are strongly correlated to transformation temperatures.[5–9]

In the previous research, the author proposed a manufacturing process for functionally graded TiNi SMAs (FGSMAs), in which the transformation temperatures change gradually within a material.[10] It is widely recognized that the Ni concentration can significantly affect the transformation temperatures in TiNi SMAs,[7,11] and this property is actively utilized. For example, if the entire material exhibits superelasticity and its deformation resistance can be graded, a guidewire with both flexibility and operability could be developed. Conversely, if the material demonstrates a shape memory effect with a gradual change in shape recovery temperature throughout, it could enable the creation of an actuator that operates independently of a power supply or sensor, with a stroke that adapts to the ambient temperature. Consequently, FGSMAs have the potential to exhibit advanced functional properties not found in conventional TiNi SMAs.

Several studies on imparting functionally graded properties to TiNi SMAs have been reported.[12] For example, Mahmud *et al.*[13] proposed a method of applying different heat treatments to various parts of cold-worked SMA wires. However, there are a few examples of realizing this in bulk form, and to the best of the author's knowledge, there are no reports detailing with the local deformation characteristics of FGSMAs.

In this study, the transformation properties, density, and hardness of the FGSMA generated by the previously indicated procedure are elucidated. In addition, while applying tensile load to the FGSMA, digital image correlation (DIC) was utilized to determine the local strain distribution throughout the material.[14] Moreover, the gradient functional characteristics of deformation resistance were examined in detail. Through these efforts, it was discovered that ultrasonic shot peening (USP) can effectively induce the gradient functional characteristics.[15]

2. Materials and Methods

2.1 Fabrication process for FGSMA

Powder metallurgy and thermomechanical treatments constitute the production process for the FGSMA proposed in this study and are essentially identical to the procedures outlined in Ref. 10. Figure 1 presents a general overview of this process. Initially, pure Ti and Ni powders with particle sizes of less than 45 μm and 3–5 μm, respectively, were utilized to produce the sintered body. The two powders were mixed using a planetary ball mill. The mixture ratio of Ti and Ni powders was adjusted such that after alloying, the Ni concentration would vary from 49.8 to 51.0 at%, in increments of 0.3 at% (a total of five types). These mixed powders were stacked in sequence in a graphite die. Subsequently, spark plasma sintering was performed at a sintering
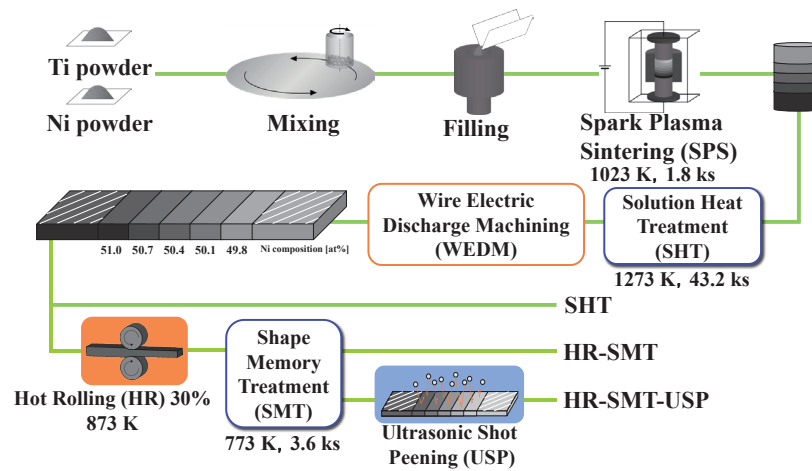
Fig. 1.   (Color online) Fabrication process for FGSMA by a combination of powder metallurgy, hot rolling, and USP treatment.

temperature of 1023 K and a holding time of 1.8 ks. During sintering, a compressive load of 10.4 kN was constantly applied in the axial direction of the powder compact to promote compaction. The resulting cylindrical sintered compact had a diameter of 20 mm and a length of 29 mm following sintering. Finally, solution heat treatment (SHT) was performed to homogenize the structures and solid solutions of Ti and Ni. The SHT was maintained at 1273 K for 43.2 ks in Ar atmosphere, followed by furnace cooling. Afterward, wire electrical discharge machining was used to remove plate-shaped specimens, which measured a total of 29 mm in length, 5 mm in width, and 1.1 mm in thickness, from the sintered compact. The Ni concentration in the plate-shaped specimen progressively varied along its longitudinal direction. The length of each region corresponding to a Ni concentration was set to 3 mm, and the ends were set to 7 mm to serve as grips during tensile testing. The specimens produced by the aforementioned procedure are collectively referred to as SHT specimens.

Each SHT specimen was subsequently subjected to hot rolling for densification, which was conducted at 873 K. The reduction rate (thickness reduction rate) R is defined as

$$R = \frac{t_0 - t_1}{t_0} \times 100 \ (\%).$$

(1)

Here, t_0 represents the thickness before rolling (SHT specimen) and t_1 the thickness after rolling. In this study, $R = 30\%$ was achieved through multiple hot rolling processes. The shape memory properties were then added to the hot-rolled plate by shape memory heat treatment. During this heat treatment, the shape that was to be memorized was restrained to be flat. The temperature for the shape memory heat treatment was 773 K, the holding time was 3.6 ks, and the cooling

method was water cooling. The material treated up to this point is referred to as the HR-SMT specimen. To achieve work hardening and compressive residual stress in the plate material that underwent shape memory heat treatment, levels for the amplitude of the vibration tool and the coverage of USP are also set under the conditions summarized in Table 1. The material subjected to USP treatment is denoted as the HR-SMT-USP specimen.

2.2 Tension test

Tension tests were conducted to investigate the overall deformation characteristics and local deformation properties of FGSMAs. DIC was used to measure local strains during loading and unloading. The specimens were captured using a digital camera and DIC analysis was performed using still images extracted from the recorded videos. Tension tests were conducted at room temperature using a Shimadzu Ez-graph testing machine, and a Nikon D5300 camera was used for image acquisition.

Specimens with random patterns were prepared for DIC analysis. Initially, each specimen was completely coated with black spray paint, and then a random pattern was created by spray painting in white. Using the digital images captured before and after deformation, this random pattern made it possible to accurately analyze the strain distribution. A sample image of the specimen used for DIC is shown in Fig. 2.

During the tension test, the crosshead displacement δ and gauge length L were used to calculate the whole strain δ/L. The loading rate was set to a strain rate of 1%/min. The maximum strain reached $\delta/L = 6\%$, after which unloading was performed at a rate of 1%/min. Subsequently, the specimens were heated under stress-free conditions to examine shape-recovery strain, with the heating temperature exceeding the reverse transformation finish temperature.

Table 1
USP treatment conditions.

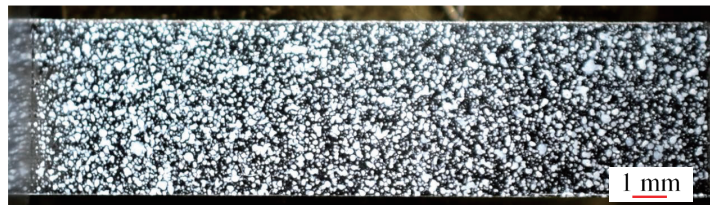| Shot media		Amplitude of vibration tool	Coverage
Material	Diameter		
52100 / AISI (SUJ2 / JIS)	0.8 mm	70 μm	1000% (200 s)

Fig. 2.   (Color online) Image of random-patterned specimen.

3. Results and Discussion

3.1 Density and hardness

The results of the investigation of density variations during the fabrication process, as described in the previous section, are shown in Fig. 3. The plotted data represent the average density and R of the ten test specimens. The horizontal error bars indicate the maximum and minimum R values during hot rolling, whereas the vertical error bars represent the maximum and minimum densities. The secondary vertical axis shows the relative density calculated from the measured density of the cast TiNi SMA (6.44 g/cm³). Figure 3 shows that the density increases steadily up to R of 20%. However, beyond 20%, the rate of increase slightly diminishes. This correlation suggests a significant relationship between density and R. The results in Fig. 3 reveal a significant increase in density after hot rolling, from approximately 5.9 g/cm³ to 6.3 g/cm³ (corresponding to a relative density of approximately 92 to 98%). This substantial increase indicates the densification effect of hot rolling. After the USP treatment, there is a slight increase in the rolling reduction and density. In contrast, during shape memory heat treatment, R (in this case, corresponding to the reduction in specimen thickness after rolling) experiences a slight decrease. This phenomenon results from the expansion of voids that were initially compressed during rolling or USP treatment, triggered by shape recovery during heating.

The Vickers hardness of the specimens subjected to each procedure is shown in Fig. 4. The Ni compositions shown in this figure are ideal values within a predefined region, and these are assumed to remain unchanged during each fabrication process. All fabrication procedures resulted in an increase in the Vickers hardness within the regions that correspond to the various amounts of Ni. Densification during hot rolling and work hardening during USP treatment were the primary causes of this increase in hardness. Furthermore, focusing on the Vickers hardness in each Ni concentration region, a phenomenon of increasing hardness with increasing Ni concentration was observed at various stages of the manufacturing process. This phenomenon was closely related to the local deformation characteristics discussed in Sect. 3.5.

3.2 Distribution of concentration

Micro X-Ray fluorescence (M4 TORNADO PLUS, BRUKER) analysis was performed to clarify the concentration distribution of Ni and Ti in the HR-SMT specimen. The results of the compositional analysis are shown in Fig. 5. Figure 5(a) shows an optical image of the entire specimen, and Fig. 5(b) shows an enlarged optical image of the analysis area. Figure 5(c) shows the distribution of Ni and Fig. 5(d) shows that of Ti, with brighter areas indicating a higher proportion of the corresponding element. Figure 5 qualitatively reveals that the Ni concentration is lower and that of Ti is higher on the 49.8 at% Ni side, but the distributions of Ni and Ti are nonuniform even within the same concentration region. It is also observed that the Ti concentration tends to be lower where the Ni concentration is locally higher.

This study indicates that the Ni concentration decreases globally towards the side with lower Ni concentration. Conversely, it is necessary to achieve a more uniform concentration of each
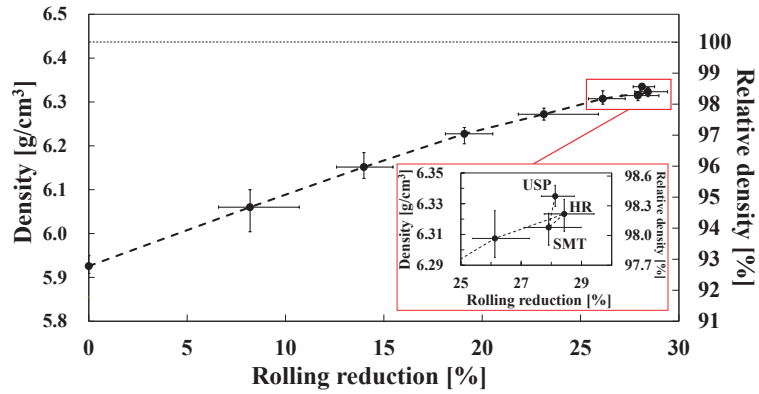
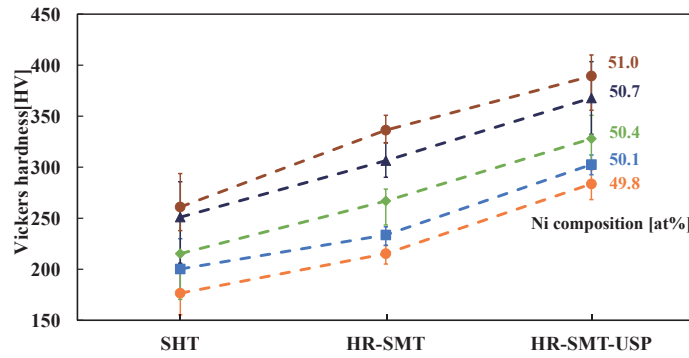Fig. 3.   (Color online) Density changes of FGSMA with processing.

Fig. 4.   (Color online) Change in Vickers hardness of FGSMA with processing.
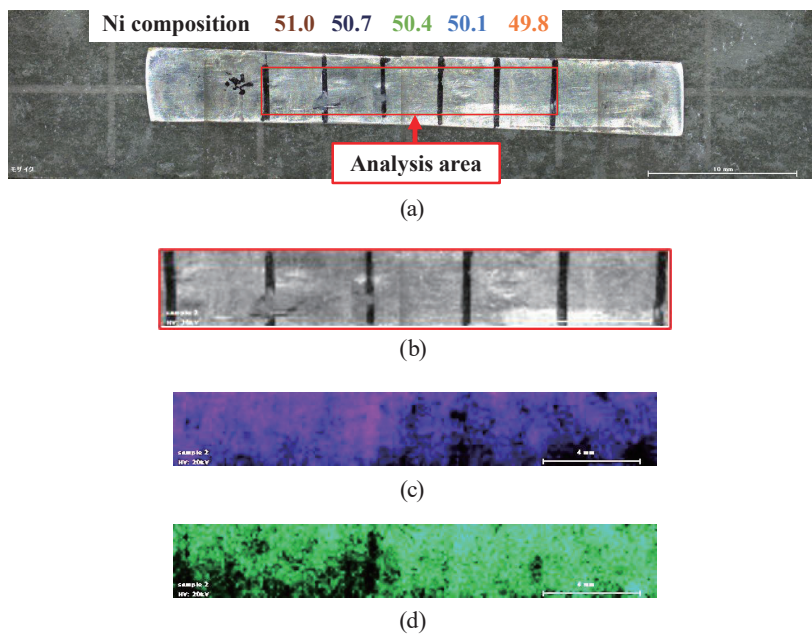

(a)

(b)

(c)

(d)

Fig. 5.   (Color online) Concentration distributions determined by micro X-Ray fluorescence analysis: (a) optical image of entire specimen, (b) enlarged optical view of analysis area, and distributions of (c) Ni and (d) Ti.

element to ensure a uniform deformation of the material within the same Ni concentration region. This aspect will require further investigation in the future.

3.3 Transformation characteristics

For HR-SMT and HR-SMT-USP specimens, differential scanning calorimetry (DSC) measurements were conducted to elucidate the transformation characteristics at positions corresponding to each Ni concentration. The resulting DSC curves are shown in Figs. 6 and 7, respectively. In both figures, (a) shows the cooling process, while (b) shows the heating process. In addition, the transformation temperatures obtained from the DSC curves are summarized in Tables 2 and 3.

In Figs. 6 and 7, particularly in the low Ni concentration region, the peaks associated with the martensitic transformation and its reverse transformation are separated into two distinct peaks. To distinguish these peaks, the peak on the low-temperature side is labeled with the subscript 1 and the peak on the high-temperature side is labeled with the subscript 2. These figures show that, for both materials, as the Ni concentration increased, the transformation temperatures shifted toward lower values. This finding aligned with the general characteristics of TiNi SMAs.

Considering the phase separation into high- and low-temperature phases mentioned earlier, the increase in Ni concentration results in a larger volume of phase transformation at low temperatures and a smaller volume of phase transformation at high temperatures. In addition, both materials exhibit peaks associated with the rhombohedral phase (R phase), an intermediate phase between the martensitic and austenitic phases.
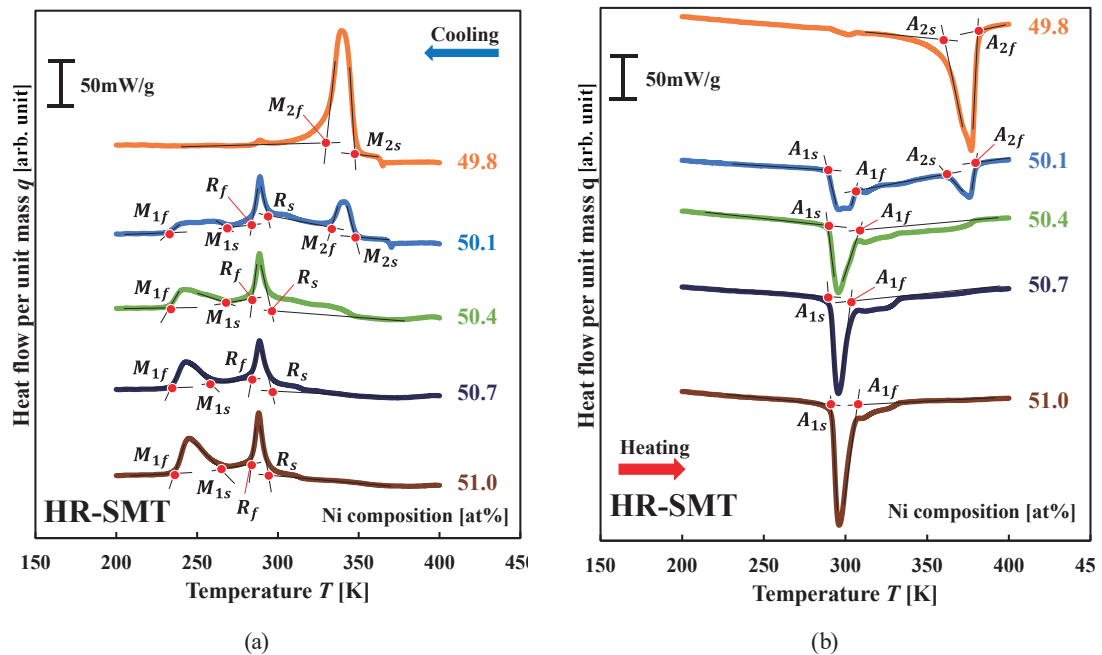

Fig. 6.   (Color online) DSC curves of HR-SMT specimen during (a) cooling and (b) heating at various Ni concentrations.
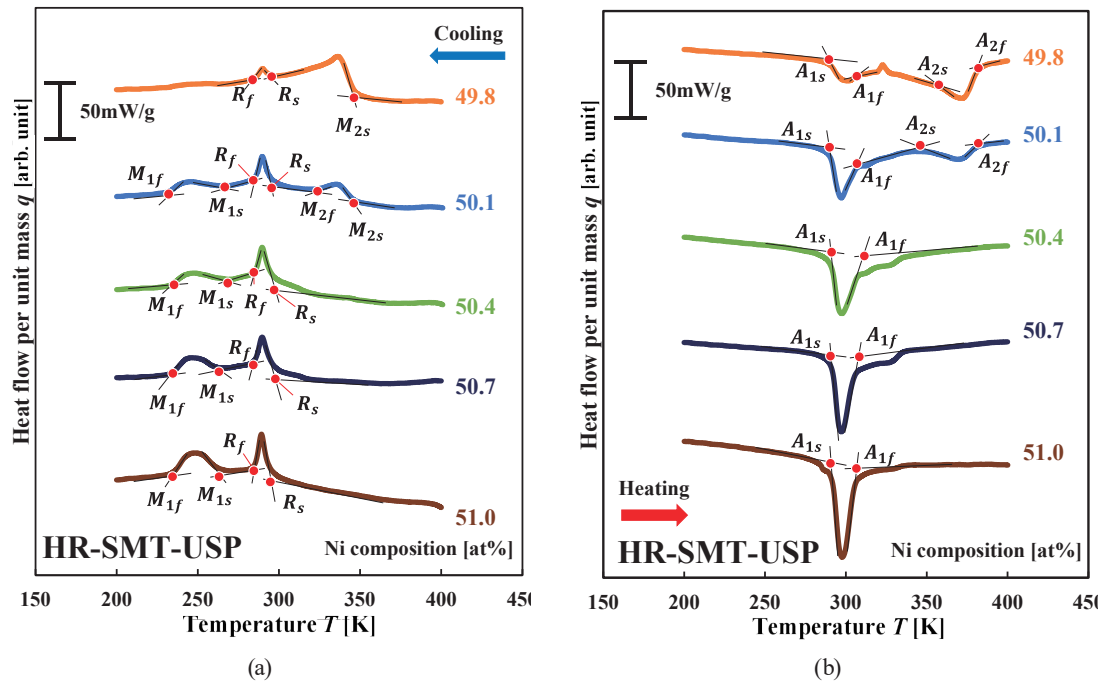
Fig. 7. (Color online) DSC curves of HR-SMT-USP specimen during (a) cooling and (b) heating at various Ni concentrations.

Table 2
Transformation temperatures of HR-SMT specimen at each Ni concentration position.

Ni concentration (at%)	Transformation temperatures (K)									
	M_{1f}	M_{1s}	R_f	R_s	M_{2f}	M_{2s}	A_{1s}	A_{1f}	A_{2s}	A_{2f}
49.8	—	—	—	—	331	348	—	—	361	381
50.1	232	269	285	294	334	348	289	306	362	380
50.4	233	268	285	296	—	—	290	309	—	—
50.7	235	259	284	296	—	—	290	303	—	—
51.0	236	262	284	294	—	—	292	306	—	—

Table 3
Transformation temperatures of HR-SMT-USP specimen at each Ni concentration position.

Ni concentration (at%)	Transformation temperatures (K)									
	M_{1f}	M_{1s}	R_f	R_s	M_{2f}	M_{2s}	A_{1s}	A_{1f}	A_{2s}	A_{2f}
49.8	—	—	283	296	—	348	290	301	360	383
50.1	231	266	285	296	324	351	290	307	351	383
50.4	233	266	285	296	—	—	291	311	—	—
50.7	234	262	285	298	—	—	291	307	—	—
51.0	234	264	285	296	—	—	291	307	—	—

Next, the changes in transformation characteristics due to the USP treatment are discussed. From the DSC curves of the cooling and heating processes in Figs. 6 and 7, it is observed that while significant changes do not appear on the high Ni concentration region upon USP treatment, there is a slight broadening tendency in the low Ni concentration region. However, overall, the

flattening of the peaks after USP treatment was minimal. Unlike conventional plastic deformation, phase changes were not inhibited by the conditions employed for USP treatment. Despite the improvement in Vickers hardness observed at each Ni concentration attributed to the USP treatment (Fig. 4), the lack of significant changes in transformation characteristics suggests differences in the evaluation regions in each experiment. The Vickers hardness test evaluates the surface properties, whereas DSC evaluates the overall transformation characteristics, regardless of the position in the thickness direction. Therefore, the results shown in Figs. 6 and 7 suggest that the layer affected by the USP treatment remains confined to a shallow region near the surface.

3.4   Residual stress

The effect of USP treatment on the residual stress distribution in the thickness direction at the position corresponding to 51.0 at% Ni concentration was quantitatively examined. The obtained results are shown in Fig. 8, indicating that the HR-SMT specimen, corresponding to the state before USP treatment, does not exhibit compressive residual stress regardless of depth. However, for the HR-SMT-USP specimen, a compressive residual stress of approximately 300 MPa was observed at a depth of 20 μm, and this stress gradually decreased with increasing depth. These results demonstrate that the USP treatment on the surface of the TiNi SMA produced by this procedure is effective in introducing compressive residual stress.

3.5   Deformation property

The stress–strain curves for HR-SMT and HR-SMT-USP specimens, as obtained through DIC, are shown in Fig. 9. The horizontal axis in this figure represents the average local strain ε_x along the specimen's axial (longitudinal) direction, which corresponds to each Ni concentration region. In these curves, stress plateaus are observed in both materials during loading; these are
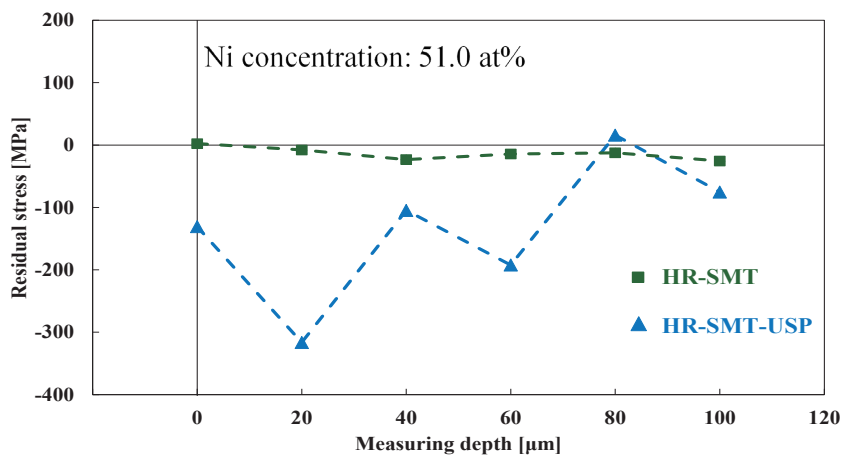

Fig. 8.   (Color online) Depth profiles of residual stress in HR-SMT and HR-SMT-USP specimens.
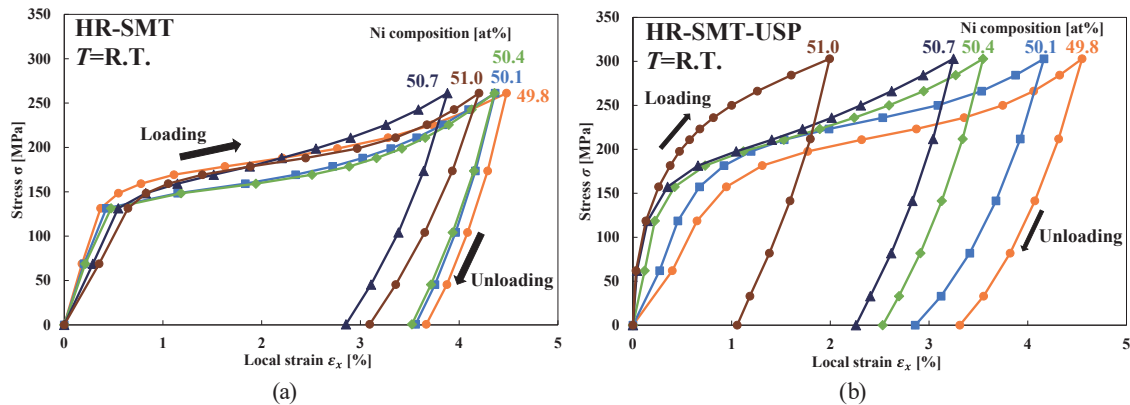
Fig. 9.   (Color online) Stress–local strain curves at each area of Ni concentration in (a) HR-SMT and (b) HR-SMT-USP specimens, obtained by DIC.

characteristics of TiNi SMAs and are attributed to stress-induced martensitic transformations or the rearrangement of martensite variants. Notably, compared with the HR-SMT specimen, the HR-SMT-USP specimen typically exhibits higher stress levels of plateaus. This difference is attributed to the work hardening induced by USP treatment. As shown in Fig. 9(a), the HR-SMT specimen does not exhibit a functionally graded behavior of deformation resistance. However, for the HR-SMT-USP specimen, the stress level increases with the Ni concentration, and the maximum strain tends to decrease, resulting in a clear manifestation of the functionally graded behavior of deformation resistance. This trend aligns with the well-known characteristics of TiNi SMAs, where increasing the Ni concentration leads to greater deformation resistance. As observed in Figs. 4 and 7, an increase in Ni concentration results in a higher Vickers hardness and lower transformation temperatures. This pattern suggests that the material exhibits more prominent superelastic deformation properties as the deformation resistance increases in the high Ni concentration region. Therefore, the local deformation characteristics of the HR-SMT-USP specimen align with these known properties and trends. Figure 9 also shows that elastic deformation appears in the initial stage of tensile loading and that the elastic modulus increases with the Ni concentration. This is due to the difference in phase at room temperature where the tensile tests were performed. As shown in Fig. 7, the material is in the austenite phase in the high Ni concentration region and in the martensitic phase in the low Ni concentration region at room temperature. The lower elastic modulus of the martensitic phase is believed to be the reason for this difference.[7] However, there may be other reasons for such large differences, and clarifying this point is a subject for future research. Notably, both materials exhibit nearly complete strain recovery upon heating after unloading.

For a quantitative examination, the local strain distributions along the central axis are measured in the HR-SMT-USP specimen, and the results are shown in Fig. 10. This figure shows the local strain distributions during loading (σ = 195 MPa), at maximum stress, and after unloading. At maximum stress, the local strain changes within the material and decreases with high Ni concentration, which is consistent with the local deformation characteristics observed in Fig. 9. The fluctuation in local strain is likely affected by the Ni concentration variations as
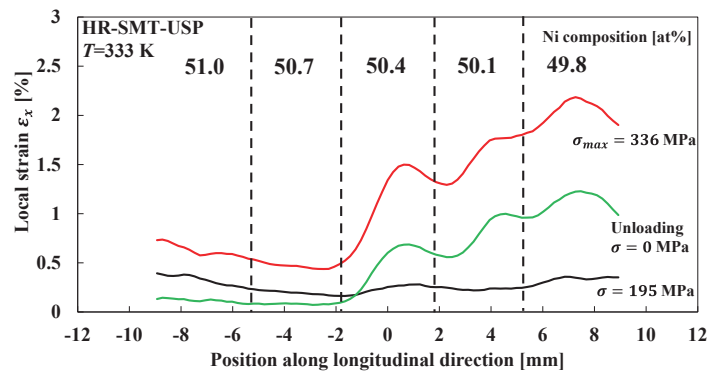
Fig. 10.   (Color online) Longitudinal local strain distribution in HR-SMT-USP specimen, obtained by DIC.
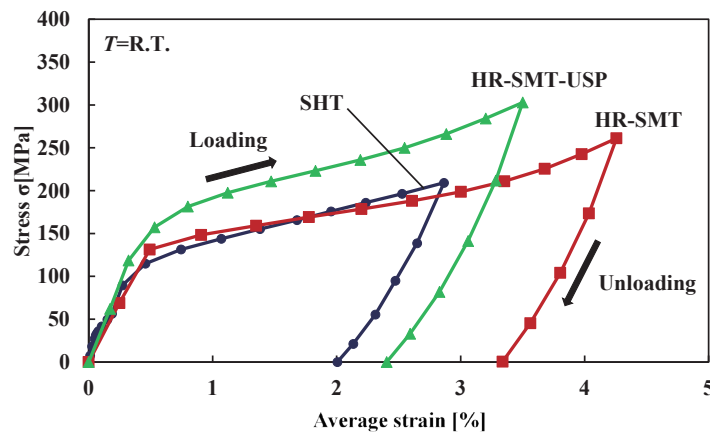

Fig. 11.   (Color online) Stress–average strain curves for each material, obtained by DIC.

discussed in Sect. 3.2 and the distribution of small voids, but further detailed investigation is necessary.

The stress–strain diagrams for SHT, HR-SMT, and HR-SMT-USP specimens are shown in Fig. 11. The horizontal axis represents the average local strain ε_x across the entire specimen, determined by DIC. Although the maximum strains for the three materials do not coincide, this discrepancy arises because the maximum strain is defined using the strain δ/L obtained from the crosshead displacement. As shown in Fig. 11, the HR-SMT specimen has a slightly higher stress than the SHT specimen at the beginning, but there is little difference in stress level between the two during the stress plateau. Dislocations are not considered to exist because the hot rolling was at a sufficiently high temperature of 873 K. Therefore, the primary difference between the two lies in their densities. This is because denser materials have fewer voids, preventing microscopic stress concentrations. As shown in Fig. 3, the absolute density of the HR-SMT specimen is approximately 0.4 g/cm³ higher than that of the SHT specimen (approximately 5 points higher in relative density). However, in this study, the observed density difference did not significantly affect the deformation characteristics.

4. Conclusions

In this study, the author proposed FGSMAs to expand the application range of TiNi SMAs. The manufacturing process primarily involved powder metallurgy, hot rolling, and USP treatment as the main steps. The author revealed the effects of hot rolling and USP treatment by carefully examining the properties of every specimen fabricated by this proposed method. The main findings obtained in this study are as follows.

(1) USP treatment and hot rolling increase the Vickers hardness. The maximum increase a in Vickers hardness are approximately 80 for hot rolling and 60 for USP treatment. Hot rolling mostly resulted in densification, while USP treatment induced work hardening, leading to increased hardness.

(2) The USP treatment can introduce a compressive residual stress of up to 300 MPa on the surface of TiNi SMA sintered bodies.

(3) The transformation peaks in DSC curves shifted toward lower temperatures as the Ni content increased. This pattern was consistent with the well-known properties of TiNi SMAs. The USP treatment had no effect on the transformation characteristics of the FGSMA.

(4) The USP treatment work-hardened the sintered TiNi SMA produced through hot rolling. Martensitic transformation stress increases up to 100 MPa by USP treatment. The effect was more pronounced in the high Ni concentration region and resulted in the prominent appearance of the functionally graded behavior of deformation resistance.

References

1　J. A. Shaw and S. Kyriakides: J. Mech. Phys. Solids **43** (1995) 1243. https://doi.org/10.1016/0022-5096(95)00024-D
2　K. Tanaka, S. Kobayashi, and Y. Sato: Int. J. Plast. **2** (1986) 59. https://doi.org/10.1016/0749-6419(86)90016-1
3　J. M. Jani, M. Leary, A. Subic, and M. A. Gibson: Mater. Des. **56** (2014) 1078. https://doi.org/10.1016/j.matdes.2013.11.084
4　H. Tobushi, K. Date, and K. Miyamoto: J. Solid Mech. Mater. Eng. **4** (2010) 1094. https://doi.org/10.1299/jmmp.4.1094
5　E. A. Pieczyska, H. Tobushi, S. P. Gadaj, and W. K. Nowacki: Mater. Trans. **47** (2006) 670. https://doi.org/10.2320/matertrans.47.670
6　E. A. Pieczyska, S. P. Gadaj, W. K. Nowacki, and H. Tobushi: Exp. Mech. **46** (2006) 531. https://doi.org/10.1007/s11340-006-8351-y
7　K. Otsuka and X. Ren: Prog. Mater. Sci. **50** (2005) 511. https://doi.org/10.1016/j.pmatsci.2004.10.001
8　H. Miki, K. Tsuchiya, M. Ohtsuka, M. Gueltig, M. Kohl, and T. Takagi: Advances in Shape Memory Alloy, Q. Sun, R. Matsui, K. Takeda, and E. A. Pieczyska, Eds. (Springer International Publishing, Cham, 2017) Chap. 11. https://doi.org/10.1007/978-3-319-53306-3_11
9　H. Tobushi, R. Matsui, K. Takeda, and E. A. Pieczyska: Mechanical Properties of Shape Memory Materials (Nova Science Publishers, New York, 2013) Chap. 1. https://novapublishers.com/shop/mechanical-properties-of-shape-memory-materials/

10   R. Matsui, K. Takeda, and H. Tobushi: Advances in Shape Memory Alloy, Q. Sun, R. Matsui, K. Takeda, and E. A. Pieczyska. Eds. (Springer International Publishing, Cham, 2017) Chap. 10. https://doi.org/10.1007/978-3-319-53306-3_10

11   J. Frenzel, E. P. George, A. Dlouhy, Ch. Somsen, M. F.-X. Wagner, and G. Eggeler: Acta Mater. **58** (2010) 3444. https://doi.org/10.1016/j.actamat.2010.02.019

12   B. S. Shariat, Q. Meng, A. S. Mahmud, Z. Wu, R. Bakhtiari, J. Zhang, F. Motazedian, H. Yang, G. Rio, T. Nam, and Y. Liu: Mater. Des. **124** (2017) 225. https://doi.org/10.1016/j.matdes.2017.03.069

13   A. S. Mahmud, Y. Liu, and T. Nam: Smart Mater. Struct. **17** (2008) 015031. https://doi.org/10.1088/0964-1726/17/01/015031

14   T. C. Chu, W. F. Ranson, and M. A. Sutton: Exp. Mech. **25** (1985) 232. https://doi.org/10.1007/BF02325092

15   M. Rakita, M. Wang, Q. Han, Y. Liu, F. Yin: Int. J. Comput. Mater. Sci. Surf. Eng. **5** (2013) 189. https://doi.org/10.1504/IJCMSSE.2013.056948